

See discussions, stats, and author profiles for this publication at: <https://www.researchgate.net/publication/231642656>

Catalytic Effect of Gold Nanoparticles Self-Assembled in Multilayered Polyelectrolyte Films

ARTICLE *in* THE JOURNAL OF PHYSICAL CHEMISTRY C · JUNE 2007

Impact Factor: 4.77 · DOI: 10.1021/jp071067c

CITATIONS

54

READS

17

3 AUTHORS:



Mariana Chirea

Koc University

21 PUBLICATIONS **312** CITATIONS

SEE PROFILE



Carlos Pereira

University of Porto

108 PUBLICATIONS **1,543** CITATIONS

SEE PROFILE



A Fernando Sousa Silva

University of Porto

162 PUBLICATIONS **2,207** CITATIONS

SEE PROFILE

Catalytic Effect of Gold Nanoparticles Self-Assembled in Multilayered Polyelectrolyte Films

Mariana Chirea,* Carlos M. Pereira, and Fernando Silva

Departamento de Química da Faculdade de Ciências da Universidade do Porto, Rua do Campo Alegre, 687, 4169-007 Porto, Portugal

Received: February 7, 2007; In Final Form: April 24, 2007

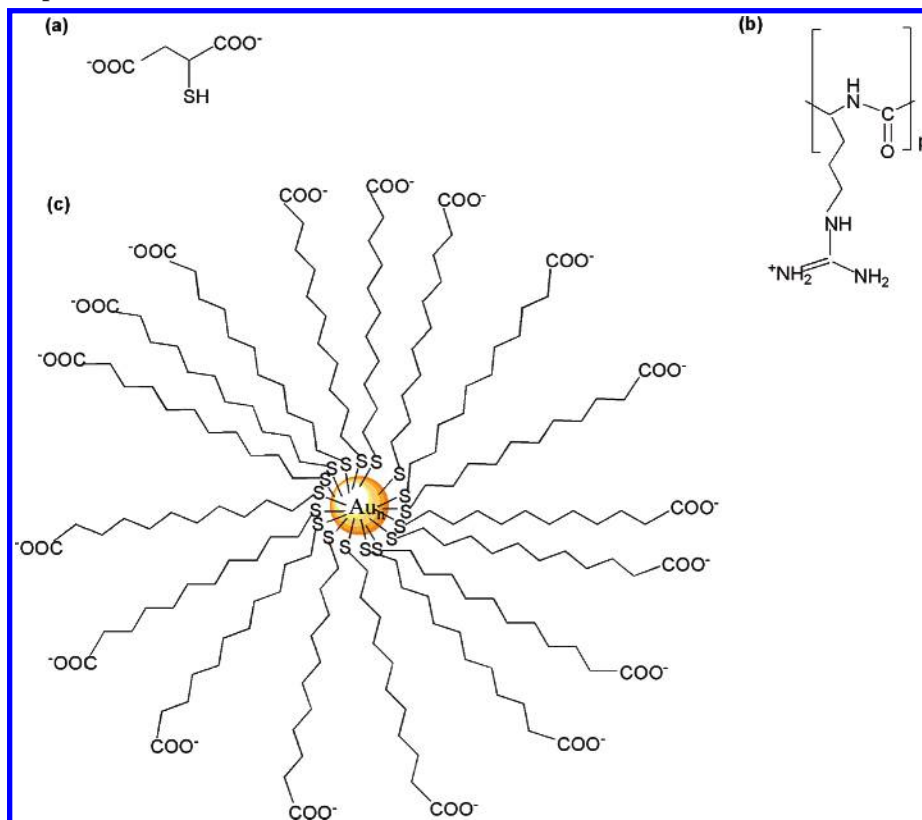
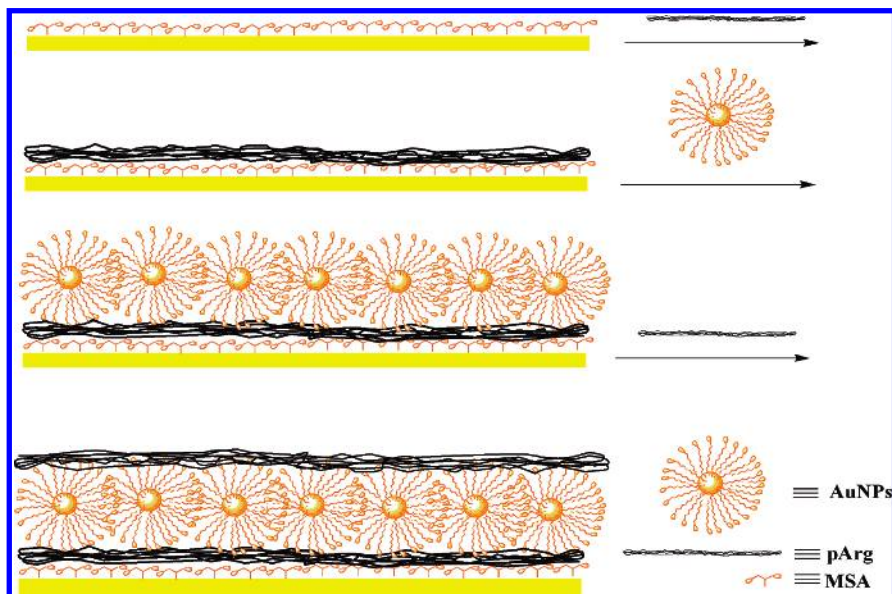
Multilayer films composed of poly(L-arginine) (pArg) and mercaptoundecanoic acid (MUA) stabilized gold nanoparticles (Au–MUA NPs) have been fabricated based on the electrostatic layer-by-layer self-assembly technique upon a gold electrode modified with a first layer of mercaptosuccinic acid (MSA). The formation of the pArg/Au–MUA NP self-assemblies as alternative multilayers was confirmed by UV–vis absorption spectroscopy and atomic force microscopy while their electrochemical properties were studied using cyclic voltammetry, square wave voltammetry, and electrochemical impedance spectroscopy. Charge transport through the multilayer was studied experimentally by using the redox pair $[\text{Fe}(\text{CN})_6]^{3-/4-}$. It was found that these new assemblies have a high permeability to the probe ions. The presence of the Au–MUA NPs greatly improves the conductivity and the electron-transfer ability of the film which exhibited new electrical properties characterized by a low impedance response and enhanced electric current as more layers were added for both Au–MUA NP and pArg terminated multilayers. It is concluded that the behavior observed is based on two cumulative contributions: electron transfer mediated by the Au–MUA NPs layers and ionic diffusion favored by the poly(L-arginine) layers due to the Donnan inclusion. The films obtained showed high conductive properties which represent very promising features for the construction of electrochemical sensors or nanoelectronic devices.

1. Introduction

From a practical point of view, the integration of metal nanoparticles into thin films is important for a wide range of applications such as chemical, electrochemical, and biological sensing^{1–7} or the construction of optoelectronic nanodevices.^{8–11} Nanomaterials exhibit unique electronic, optical, and catalytic properties due to their size, morphology, large surface area, and possible quantum confinement.^{12,13} In particular, gold nanoparticles (Au NPs) are widely used for different studies due to their chemical stability and easy preparation. Compared to bulk gold which is chemically inert,¹⁴ Au NPs exhibit an outstanding catalytic activity for various chemical and electrochemical processes. For example, Haruta and co-workers have demonstrated that gold nanoparticles (<10 nm) supported on oxides display high catalytic activity for the chemical and electrochemical oxidation of carbon monoxide (CO) and methanol.¹⁵ Caruso and co-workers have demonstrated that 4-(dimethylamino)pyridine-stabilized gold nanoparticles (DMAP–Au NP) can be utilized as efficient electrochemical sensors for the oxidation of nitric oxide (NO).¹⁶ Oshaka et al. have shown that multilayers composed of citrate stabilized Au NPs and 1,4-benzene-dimethanethiol (BDMT) catalyze the reduction of oxygen to hydrogen peroxide.⁴ Goodman and co-workers reported that the high catalytic activity of gold nanoparticles in catalyzing CO oxidation is related to the band gap of a metallic-insulator transition for particles in the range of 1–6 nm.¹⁷ The immobilization of nanoparticles on different substrates has been performed using physical deposition (e.g., spin coating and spraying^{18,19}), electrodeposition, or the layer-by-layer technique.^{20–22} The layer-by-layer self-assembly technique, based either on

hydrogen, coordination, electrostatic, or covalent binding, has been proven to be facile and very flexible in generating a wide range of organized and stable ultrathin films.^{4,8,9,23–25} This technique allows the use of a wide range of starting materials: small organic molecules or inorganic compounds, macromolecules, biomacromolecules such as proteins or DNA, and more recently functionalized nanoparticles in order to fabricate the multilayers.^{26–33} Also recently, our group has investigated the electrochemical properties of Au NPs stabilized with mercaptosuccinic acid (Au–MSA NPs) and electrostatically deposited by means of a polycation onto thiol modified gold substrates.³⁴ These nanoparticles exhibited a high electrocatalytic activity toward positively charged probes in solution. A significant increase in the cathodic peak current has been observed indicating that Au NPs achieved a good electrical communication with the underlying electrode surface. In this paper, we extend the idea of fabricating three-dimensional multilayers of Au NPs self-assembled on gold electrodes using the layer-by-layer (LbL) approach and Au NPs capped with a ligand having a longer chain. The work describes the synthesis of Au NPs stabilized with mercaptoundecanoic acid (Au–MUA NPs) and their use for the construction and characterization of layer-by-layer polymer/Au NPs self-assembled films by using poly(L-arginine) (pArg) as the polycation (see Scheme 1 which depicts the chemicals used for the multilayer buildup and Scheme 2 which illustrates the growth of the films by stepwise electrostatic adsorption of pArg and Au–MUA NPs from aqueous solution on modified gold substrates). We report here a large permeability of these assemblies to the probe ions portrayed by high peak currents observed in the cyclic and square wave voltammograms and low charge-transfer resistance as proven by the parameter values used to fit the impedance spectra. These features make the assemblies studied highly attractive for sensing and elec-

* To whom correspondence should be addressed. E-mail: mariana.chirea@fc.up.pt. Phone: +351226082934. Fax: +351226082959.

SCHEME 1: Chemical Structure of (a) Mercaptosuccinic Acid, (b) Poly(L-arginine), and (c) Gold Nanoparticles Stabilized with Mercaptoundecanoic Acid**SCHEME 2: Schematic Representation of the Layer-by-Layer Electrostatic Self-Assembly of pArg/Au–MUA NPs Multilayers**

tronic applications.^{12,13} The pArg/Au–MUA NP assemblies were characterized using UV–vis absorption spectroscopy, atomic force microscopy (AFM), cyclic voltammetry, square wave voltammetry, and electrochemical impedance spectroscopy (EIS). Charge transport through the multilayer was studied experimentally by using the redox pair $[\text{Fe}(\text{CN})_6]^{3-/4-}$. The fitting of the impedance spectra was performed using nonlinear square fit software. An excellent agreement of the experimental data and the fitted data has been obtained allowing the accurate interpretation of the EIS spectra together with an adequate electrochemical characterization of the films.

2. Experimental Section

Chemicals. The following reagents were used without further purification: hydrogen tetrachloroaurate(III) trihydrate ($\text{HAuCl}_4 \cdot 3\text{H}_2\text{O}$, 99.999%, Sigma Aldrich), methanol (CH_3OH , 99.8%, Sigma), mercaptosuccinic acid ($\text{HOOCCH}_2\text{CH}(\text{SH})\text{COOH}$, 98%, Merck), mercaptoundecanoic acid ($\text{HS}(\text{CH}_2)_{10}\text{COOH}$, 95%, Aldrich), poly(L-arginine) hydrochloride (pArg, MW = 35 000, Sigma), boric acid (H_3BO_3 p.a. quality, Riedel-de-Haën), KCl (p.a. quality, Merck), NaOH (pellets pure, Merck), potassium hexacyanoferrate(III) (p.a. quality, Merck), potassium hexacy-

TABLE 1: Size Distribution Parameters of Mercaptoundecanoic Acid Derivatized Gold Nanoparticles

sample	concn of HAuCl ₄ (M)	concn of MUA (M)	diameter (nm)	Au NPs counted	standard deviation	Au NPs dispersity (%)
a	0.0032	0.0098	1.0	659	0.18	17.6
b	0.0032	0.0064	3.0	960	0.42	14.0
c	0.0032	0.0032	3.3	1098	0.54	16.6
d	0.0064	0.0032	4.0	1023	0.71	17.0

anoferrate(II) trihydrate (p.a. quality, Merck), NaBH₄ (>96%, Merck), NaClO₄·H₂O (p.a. quality, Merck), HClO₄ (70%, redistilled, 99.999%, Aldrich), H₂SO₄ (pure, Pronalab), H₂SO₄ (pure, Pronalab), HNO₃ (69%, Pronalab), HCl (>37%, Fluka). Millipore filtered water (resistivity >18 MΩ·cm) was used to prepare all aqueous solutions and for rinsing. Before use, all the glassware was cleaned with freshly prepared aqua regia (HNO₃/HCl = 1:3, % v/v), rinsed abundantly with Millipore water, and dried.

Synthesis of Mercaptoundecanoic Acid Capped Au NPs.

The Au NPs were synthesized using a modified Kimura method,³⁵ by decreasing the molar ratio of MUA/HAuCl₄ from 3 to 0.5. The successive synthesis of Au–MUA NPs was performed using a fixed concentration of HAuCl₄ (0.5 mmol of HAuCl₄ for molar ratios S/Au of 3, 2, 1, and 1 mmol of HAuCl₄ for molar ratio S/Au of 0.5) dissolved as an 8% methanolic solution and decreased concentrations of MUA (1.5, 1.0, 0.5, and 0.5 mmol, respectively) dissolved in 150 mL of methanol. A sodium borohydride aqueous solution (25 mL and 50 mL, 0.2 M) was used for the reduction of HAuCl₄. The yellow solution of tetrachloroauric acid mixed with mercaptoundecanoic acid solution turned nontransparent orange progressively. After 15 min of strong stirring, no change in color was observed. The addition of freshly prepared 0.2 M NaBH₄, under vigorous stirring, determined the progressive change in color from nontransparent orange to dark brown to brown (S/Au of 0.5, 1, and 2, respectively) or to an orange (S/Au of 3) flocculent precipitate. After 2 h of further stirring, the solvent was removed by decantation, and the clusters obtained were purified by washing with pure methanol, 20% v/v water/methanol (200 mL) and 50% v/v water/methanol through a sonication–centrifugation process using a centrifuge (Alresa-didacen II, 4000 rpm/10 min each step) and a sonication bath (Bandeline-Sonorex), in order to remove the organic (Au–MUA complexes) and inorganic impurities (Na, Cl, B). The next step of the purification process was the precipitation of the Au–MUA NPs with HCl (0.2 M). The acidic media allow the protonation of the carboxylate groups of the MUA covalently bonded on the clusters' surface and consequently the precipitation of the nanoparticles which tend to dissolve in methanol. The HCl used for the nanoparticles' precipitation was removed by washing of the clusters with large amounts of Millipore water through sonication and centrifugation, until no precipitation of the decanted solvent by AgNO₃ was observed. The solid obtained was filtered on precut membranes with pore diameters of 0.2 μm and dried at room temperature in a desiccator for 24 h. As dry powders, mercaptoundecanoic acid derivatized gold nanoparticles were highly soluble in diluted tetraethyl ammonium hydroxide (TEAOH) aqueous solution (0.005% v/v). Au–MUA NPs dissolved in aqueous TEAOH 0.0005% showed differentiated colors depending on their size: orange for 1.0 nm average diameter (S/Au of 3), light brown for 3.0 nm average diameter (S/Au of 2), brown for 3.3 nm average diameter (S/Au of 1), and dark brown for 4.0 nm average diameter (S/Au of 0.5) (see Table 1 and Figure 1). As proven

by the ζ-potential measurements (see Table 2), the Au–MUA NPs dissolved in aqueous TEAOH were negatively charged.

Transmission Electron Microscopy. The TEM images were recorded using an electron microscope Tecnai G2 equipped with a Wolfram filament, operating at 120 kV and having a point resolution of 0.5 nm. A diluted TEAOH aqueous solution of Au–MUA NPs was dropped on Formvar copper–carbon grids followed by drying within a desiccator for 24 h. The size distribution of the Au NPs was estimated using free software, Image J.

UV–Visible Spectroscopy. The UV–vis spectra of the samples were recorded on a Hitachi U-3000 spectrophotometer in the range 200–800 nm. Quartz cuvettes with a 1 cm light path and Au–MUA NPs solution of 0.08 mg/mL in TEAOH aqueous solution (0.005% v/v) were used for the optical characterization of the NPs. Silanized quartz slides and freshly prepared pArg (1 mg/mL) and Au–MUA NPs solutions (0.85 mg/mL) were used for the multilayer buildup. The optical spectra were recorded by placing the modified quartz slides perpendicular to the beam in order to maintain the same experimental conditions for each measurement.

ζ-Potential Measurements. The ζ-potential of the nanoparticles was determined by dynamic light scattering analysis (Malvern ZetaSizer Nano series, Malvern Instruments, Malvern, Worcestershire, U.K.) using a 4 mW helium–neon laser (633 nm) as a source of incident light, operating at a scattering angle of 17° and at a temperature of 25 °C. The measurements were performed using Au–MUA NPs suspensions (0.85 mg/mL aqueous TEAOH) placed inside disposable ζ cells (Malvern ZetaSizer Nano series) successively inserted in the apparatus. The data were analyzed using standard procedures in the software provided with the instrument.

FT-IR Spectroscopy. The FT-IR spectra were recorded with a Spectrum RX I FT-IR system (Perkin-Elmer) using dry powders of gold nanoparticles and separately thiol incorporated in KBr pellets.

Gold Electrodes Preparation. The gold electrodes were cleaned as previously explained.³⁴ Briefly, the electrodes were soaked repeatedly in a 3:1 mixture of concentrated sulfuric acid and hydrogen peroxide 30% (piranha solution) for about 1 min, followed by thorough washing with large amounts of Millipore water (*Caution! Piranha solution is corrosive and reacts violently with organic materials*). Subsequently, the electrodes were polished on microcloth pads (Buehler) using a polycrystalline diamond suspension of 1 and 0.25 μm, sonicated in Millipore water for 30 min, and finally, cleaned electrochemically by cycling in a 0.02 M aqueous solution of HClO₄ at a scan rate of 100 mV/s, between the potentials −0.4 and 1.5 V vs Ag/AgCl/KCl (3 M).

Synthesis of pArg/Au–MUA NP Films. Freshly cleaned gold electrodes were immersed in a methanolic solution (10 mM) of MSA for 18 h, followed by immersion in a basic solution (0.2 M NaOH) for 10 min (in order to deprotonate the COOH groups of the thiol) and washed with Millipore water. Successively, the modified electrodes were immersed for 1 h in a boric buffer solution (pH 9) of poly(L-arginine) (pK_a ~ 12), 1 mg/mL, consecutively washed, and immersed in a tetraethyl ammonium hydroxide aqueous solution of Au–MUA NPs for 4 h, under intermittent stirring. The concentration of the Au–MUA NPs solution was 0.85 mg/mL in an aqueous solution of tetraethyl ammonium hydroxide (0.005% v/v, pH 10). All adsorbate solutions were prepared freshly prior to use. After every layer self-assembled on the surface, the electrodes were washed thoroughly with Millipore water for about 2 min

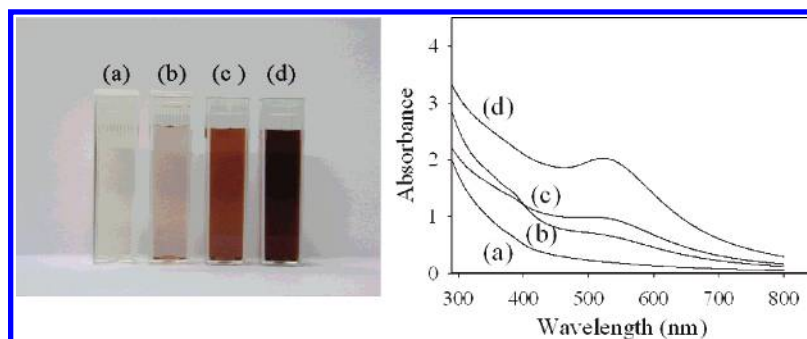


Figure 1. Mercaptoundecanoic acid derivatized gold nanoparticles solutions (left) for molar ratios of (a) S/Au of 3, (b) S/Au of 2, (c) S/Au of 1, (d) S/Au of 0.5. UV–visible spectra of the same solutions (right). The concentration was 0.08 mg/mL Au–MUA NPs in TEOAH aqueous solution (0.005% v/v).

TABLE 2: Electrophoretic Mobilities and Average Values of the ζ -Potential of Mercaptoundecanoic Acid Derivatized Gold Nanoparticles Dissolved in Aqueous TEOAH (0.005% v/v)

Au–MUA NPs diameter (nm)	average ζ -potential (mV)	electrophoretic mobilities ($\text{cm}^2/(\text{V s})$)	number of measurements
1.0	-20.6 ± 0.31	-1.61×10^{-4}	4
3.0	-29.5 ± 0.38	-2.31×10^{-4}	4
3.3	-49.3 ± 0.42	-3.83×10^{-4}	4
4.0	-58.3 ± 0.60	-4.57×10^{-4}	4

in order to remove unbound polymer or unbound Au–MUA NPs. Alternating layers of cationic poly(L-arginine) and anionic Au–MUA NPs were deposited up to a maximum of $n = 10$ layers on the electrode surface. At the pH of deposition, all adsorbates used are fully ionized ensuring a strong electrostatic interaction and allowing the growth of pArg/Au–MUA NP multilayers which proved to be mechanically robust and electrochemically stable. For the spectroscopic measurements, the buildup of the multilayers was performed on quartz slides coated with 3-aminopropyltriethoxysilane (3APTS) proceeding as explained previously.³⁴ The 3APTS treatment coats the substrates with amino groups, which allows for the buildup of the multilayers by alternately exposing the slides to the solutions of negatively charged Au–MUA NPs and positively charged poly(L-arginine). After every layer of deposition, the slides were washed with Millipore water and the UV–vis spectra were recorded between 200 and 800 nm. The absorption time for the polymer was 30 min and for Au–MUA NPs was 2 h. The spectroscopic measurements were performed in order to verify if the layers bind electrostatically between each other onto the amino silanized quartz slides. The optical and electrochemical measurements were performed twice, and the reproducibility of the results was verified.

Atomic Force Microscopy. AFM measurements were performed using a Molecular Imaging, PicoLe AFM (France). The surface topography was measured using a silicon cantilever/tip (Nanosensors) with a resonance frequency between 65 and 90 kHz. The images were scanned in topography (Figure 4), amplitude, and phase mode (results not shown) with a resolution of 512×512 pixels. Au (111) slides (Arrandee), 11 mm \times 11 mm, were used as substrates, after being cleaned with ethanol, acetone, and Millipore water and dried under nitrogen. The electrostatic adsorption of the layers was achieved using freshly prepared solutions, each adsorption step being followed by washing with Millipore water and drying of the samples under a soft flow of nitrogen. The waiting period for the electrostatic adsorption of the multilayer components and the number of layers imaged were the same as for the electrochemical

measurements. The AFM measurements were carried out twice and certified as reproducible.

Cyclic Voltammetry. Cyclic voltammetric measurements were carried out with an Autolab PGSTAT 20 potentiostat (EcoChemie B.V., The Netherlands) using a three electrode cell with a gold electrode (Radiometer Analytical, 2 mm diameter) as the working electrode, a platinum wire as the counter electrode, and an Ag/AgCl (3 M KCl) as the reference electrode (Metrohm). The electrochemical cell was enclosed in a grounded Faraday cage, and all measurements were performed at room temperature (25 °C). Nitrogen was purged in the solution about 15 min before starting each measurement and above the solution during the electrochemical measurements. Cyclic voltammograms (CVs) were measured between -0.2 and 0.6 V at a scan rate of 50 mV/s, using $[\text{Fe}(\text{CN})_6]^{3-/4-}$ as the redox probe.

Square Wave Voltammetry. Square wave voltammograms were registered with an Autolab PGSTAT 20 potentiostat (EcoChemie B.V., The Netherlands) at 10, 25, 50, 75, and 100 Hz, using a 50 mV amplitude and a 2 mV potential step.

Electrochemical Impedance Spectroscopy. Impedance spectra were recorded using a Solartron frequency response analyzer (model 1250) connected to a Solartron potentiostat (model 1287). The range of frequency used was 10 000–0.5 Hz for an amplitude of 20 mV, and a potential window around the mid-peak potential which was determined from the CVs.

3. Results and Discussion

3.1. Characterization of 11-Mercaptoundecanoic Acid Stabilized Gold Nanoparticles. The Au–MUA NPs of 1.0 nm average diameters showed no absorption peak around 500 nm in the UV–vis spectra which is consistent with previous observations³⁵ (Figure 1). Au–MUA NPs of 3.0, 3.3, and 4.0 nm average diameters showed a continuous increase of the absorption peak at about 524 nm toward higher energy, due to the collective oscillation of the electrons in the conduction band of the gold atoms, under optical excitation. The increase of the absorbance peaks confirmed the increase of the size of the nanoparticles by decreasing the S/Au molar ratio from 3 to 0.5.

The size and shape of the Au–MUA NPs were studied by transmission electron microscopy (Figure 2). In order to obtain a good statistic for the size distribution, several hundreds or thousands of particles were counted for each sample. From the TEM images in Figure 2 and the data displayed in Table 1, it was observed that the gold nanoparticles have quasispherical shapes and monodisperse sizes (polydispersity less than 20%).

Because of the purification process used and confirmed by FT-IR spectroscopy measurements, the mercaptoundecanoic acid ($\text{p}K_a \sim 7\text{--}8$) on the Au NPs surface exists in the form of a carboxylic acid (see Supporting Information, Figures S1–S5).

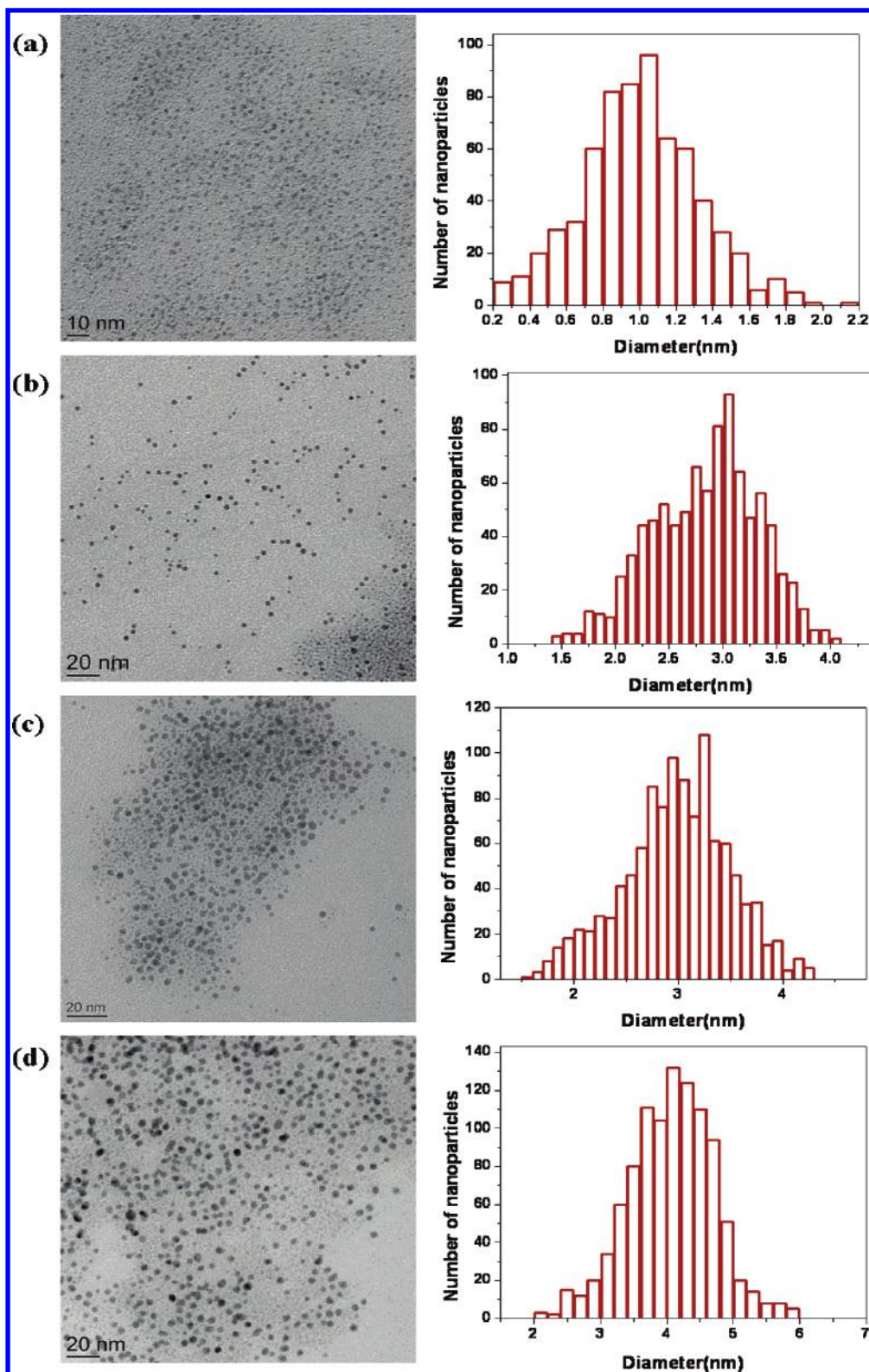


Figure 2. TEM images and size distribution histograms for Au-MUA nanoparticles of (a) 1.0, (b) 3.0, (c) 3.3, and (d) 4.0 nm average diameters.

Au NPs stabilized with MUA, as dry powders, were soluble in diluted aqueous solution of tetraethyl ammonium hydroxide which acts as a transfer agent for the nanoparticles in solution. Because the nanoparticles' surfaces are covered with carboxylic acids, it is expected that, after dissolving in the TEAOH solution (pH 10), the carboxylic groups would be changed in their corresponding carboxylate anions. To confirm this, ζ -potential measurements were performed for all the samples. The average values of the ζ -potential obtained after four consecutive

measurements for each sample are given in Table 2 and clearly show that the surface of the Au NPs was negatively charged. As observed from the synthesis method used, the molar ratios of S/Au of 2 and 1 yielded Au NPs of 3.0 and 3.3 nm average diameters, respectively. Because of the small difference between the mean average diameters of the clusters synthesized for these molar ratios, Au NPs of 3.0 nm were used for further studies.

As seen in the literature, Au-MUA NPs have been synthesized either using the Schiffrin method together with the heat

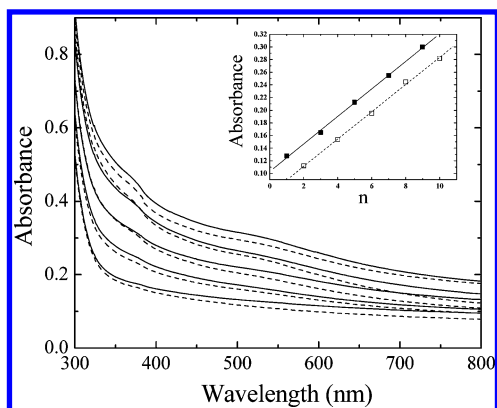


Figure 3. UV-vis spectra of the multilayer composite: solid lines for odd n (Au-MUA NP terminated multilayers) and dashed lines for even n (pArg terminated multilayers) from bottom to top. Inset: absorbance at 533 nm. Au-MUA NPs average diameters were 3.0 nm.

treatment method in order to increase the size of the nanoparticles³⁶ or by a one single phase method resulting in Au-MUA NPs of 5.0 nm average diameters.³⁷ The synthetic method used in this work yielded Au NPs of three different sizes, covered by carboxylic acids, which after purification and drying were soluble in an aqueous solution of TEAOH. By the heat treatment method, part of the COOH groups on the Au-MUA NPs surface suffered decomposition,³⁶ while by the latter method it is mentioned that the Au-MUA NPs of 5.0 nm average diameters are water soluble.³⁷ On the basis of the ζ -potential measurements performed after the purification of the Au-MUA NPs, it was observed that, apparently, the Au NPs are soluble in water but they suffer from easy aggregation. This is due to the nature of the ligand on their surface which is not soluble in water. After purification and drying, the powders were highly soluble in aqueous TEAOH, and their stability is a function of the nanoparticles size as follows: Au-MUA NPs of 1.0 nm average diameters were stable for about 6 h, the Au-MUA NPs of 3.0 and 3.3 nm average diameters were stable for about 3–4 days, while the Au-MUA NPs of 4.0 nm average diameters were stable for about 1 week without visible aggregation. The TEAOH acts as a transfer agent increasing the nanoparticles' stabilities in aqueous solution.

3.2. Characterization of Poly(L-arginine)/Au-MUA NP Multilayers. In the following discussion, n denotes the number of layers. For the electrochemical measurements performed for the redox pair $[\text{Fe}(\text{CN})_6]^{3-/4-}$, the bare electrode corresponds to $n = 0$, and the first negatively charged MSA layer corresponds to $n = 1$. Then, even n values correspond to positively charged, pArg terminated multilayers. Odd n (≥ 3) values correspond to negatively charged Au-MUA NPs terminated multilayers.

UV-Vis Spectroscopy. Figure 3 shows the optical spectra of the multilayer built up on silanized quartz slides using Au-MUA NPs with 3.0 nm average diameters as the polyanion and poly(L-arginine) as the polycation. The gold colloids used in our work have a sensitive surface plasmon absorption band at about 524 nm (as shown in Figure 1), which was used to monitor the growth of the layers and the assembly process of the pArg/Au-MUA NP film. The absorbance at the surface plasmon band increased linearly with the numbers of the attached Au-MUA NPs (solid lines) and pArg layers (dotted lines) in the film (inset of Figure 3), which indicated a progressive and uniform deposition process of the pArg/Au-MUA NPs multilayer and suggested that the amounts of adsorbed Au-MUA NPs and pArg in the assembly process were essentially the same for each layer. The first layer electrostatically adsorbed on the modified

quartz slides was a Au NPs layer (in Figure 3, from bottom to top, the first solid line) characterized by an increase of the absorbance value compared to the silanized quartz slide (spectrum not shown). The next deposited layer was the poly(L-arginine) (in Figure 3, from bottom to top, the first dashed line) which caused a decrease of the scattering of light of the previously deposited Au NP layer and consequently a decrease of the absorbance value. The third layer electrostatically adsorbed was a Au NPs layer (in Figure 3, from bottom to top, the second solid line) which as expected caused an increase of the scattering of light and consequently an increase of the absorbance values due to the increasing amount of nanoparticles in the film. Successively, as more layers were built up, each polymer layer determined a slight decrease of the absorbance values of the previously deposited Au NPs layer, but overall the absorbance increased as the quantity of nanoparticles deposited within the film increased.

In addition, a red-shift of the surface plasmon from 524 to 533 nm was observed along with the multilayer buildup. This is due to a reduced nanoparticle-nanoparticle distance (i.e., more dense packing) in the film as compared with that of Au-MUA NPs dispersed in an aqueous TEAOH solution (0.005% v/v). This is consistent with previous observations for Au NPs having similar or bigger diameters for which the surface plasmon band is well defined, and the reduced distance between nanoparticles determines the shift of this band toward higher wavelengths.¹⁰ The systematic layering within the multilayer was confirmed also by AFM measurements performed for all the three types of synthesized colloids.

Atomic Force Microscopy. The changes of the topography for each layer of deposition on gold slides were investigated by tapping mode AFM. The scan size was 1 μm for all the images. As seen in our previous work,³⁴ the small molecule of the MSA chemisorbed on a clean Au (111) slide (Supporting Information, Figure S6a) determined no change in the topography (rms 2.82 nm) while the first poly(L-arginine) layer showed uniform distribution on the slide and slightly decreased surface roughness compared with the MSA layer (rms of 2.41 nm, Figure S6b). Figure 4 shows the topographic images of the following steps of the buildup process: successively electrostatic adsorbed Au-MUA nanoparticles of 3.0 nm average diameters (Figure 4c,e,g,i) and poly(L-arginine) (Figure 4d,f,h,j). Also, comparative studies were performed under the same conditions for multilayers containing clusters of 1.0 and 4.0 nm average diameters (see Supporting Information, Figure S7 showing pArg as the fourth layer and Au-MUA as the fifth layer within the multilayer composites). In all cases, two different topographies were observed: small spheroids, as it could be expected, for the outermost Au-MUA NPs layers (Figure 4c,e,g,i and Figure S7n,p,r) and a flat topography for poly(L-arginine) as the outermost layers (Figure 4d,f,h,j and Figure S7m,o,q).

These structures were superimposed upon one another as more layers were deposited, thus indicating the complexation between the polymer and the Au-MUA NPs. For these types of layers, the growth was more uniform than for poly(L-lysine)/mercaptosuccinic derivatized gold nanoparticles multilayers studied in our previous work.³⁴ This could be due to the longer chain of the MUA on the Au cluster surface which facilitates the electrostatic binding between the Au NPs and the poly(L-arginine). The pArg/Au-MUA NP multilayer containing clusters of a 1.0 nm mean diameter showed a thinner film growth compared with the other two multilayers, which could be due to the small size of the nanoparticles used (Figure S7m,n). The

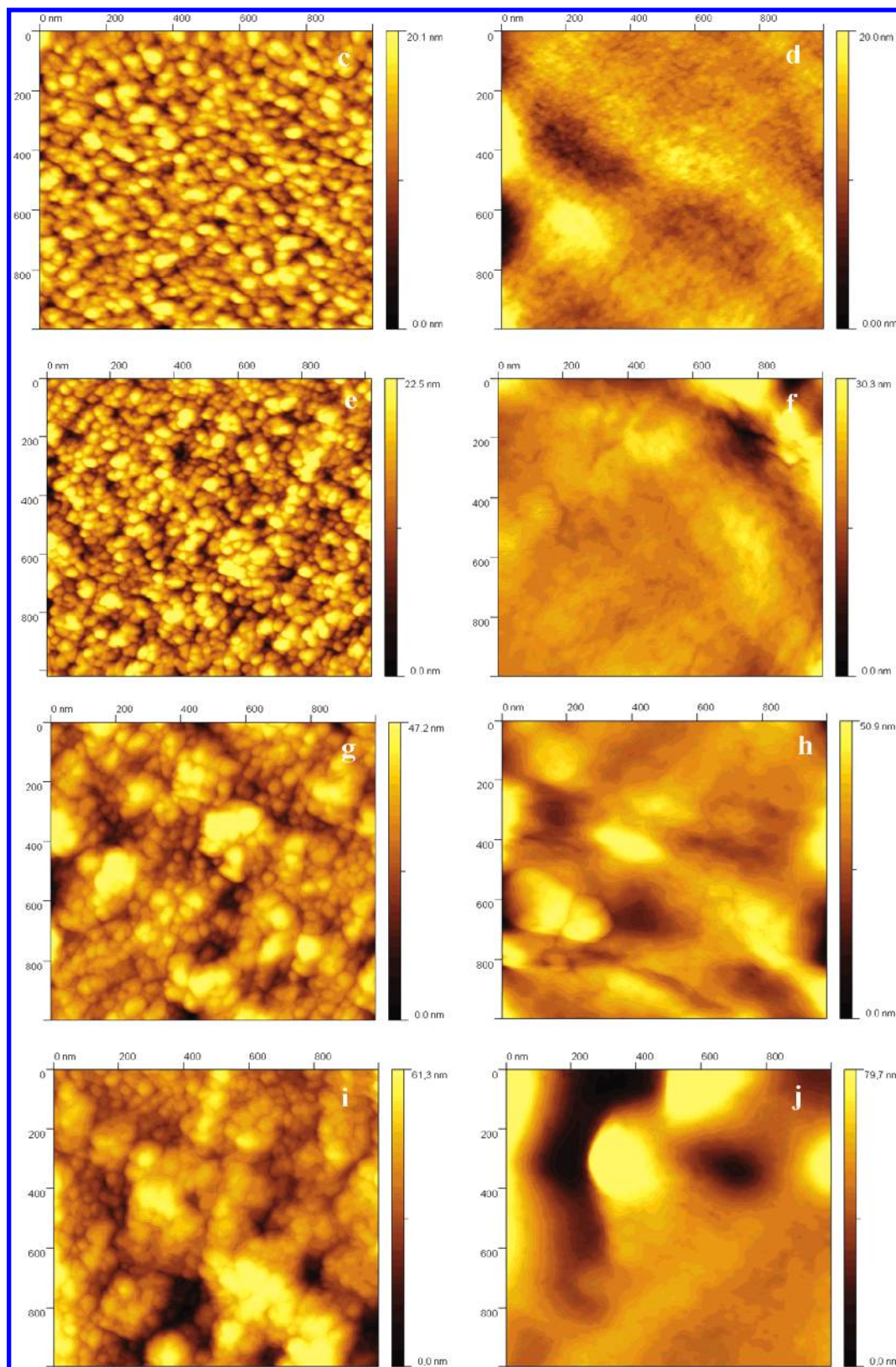


Figure 4. Topographic tapping mode AFM images of the multilayer composite: (c, e, g, i) Au-MUA NP terminated multilayers with $n = 3, 5, 7$, and 9 layers, respectively; (d, f, h, j) pArg terminated multilayers with $n = 4, 6, 8$, and 10 layers, respectively. The clusters used were 3.0 nm average diameters.

root-mean-squared roughness determined from the AFM images showed that the gold nanoparticles tend to slightly increase the roughness of the surface while the poly(L-arginine) has a strong effect of softness (see Table 3 and Supporting Information, Table S1). This is in contrast with our previous work³⁴ where the poly(L-lysine) determined an increase of the rms parameter while

the mercaptosuccinic stabilized gold nanoparticles were embedded in the polymer matrix inducing a decrease of the topography roughness. The multilayer composed of Au-MUA NPs of 1.0 nm and poly(L-arginine) showed less defects, pinholes, and preferential paths for diffusion and a coalescence of the structural elements after the seventh layer electrostatically adsorbed on

TABLE 3: Root-Mean-Squared Roughness Corresponding to the Topographic Tapping Mode AFM Images in Figure 4^a

<i>n</i>	rms (nm)
1	2.82
pArg Layers	
2	2.41
4	1.62
6	3.53
8	7.27
10	9.30
Au–MUA Layers	
3	3.21
5	4.10
7	7.77
9	11.42

^a See Supporting Information for the topographic tapping mode AFM images of MSA (*n* = 1, Figure S6a) and the first poly(L-arginine) layer (*n* = 2, Figure S6b).

the slides (result not shown). The very bright spots in Figures 4 and S7 arise from the maximization of the contrast in the AFM images, which was purposely done in order to optimize the image quality. The multilayer composed of Au–MUA NPs of 3.0 nm mean diameter and poly(L-arginine) showed uniform distribution for both of the Au NPs layers and the poly(L-arginine) layers, few pinholes and defects as more layers were adsorbed, a well-packed structure starting the third layer, and progressively a more compact structure with increased roughness and darker spots starting the seventh layer electrostatically adsorbed on the gold slides (Figure 4). The multilayer composed of Au–MUA NPs of 4.0 nm mean diameter and poly(L-arginine) (Figure S7q,r) showed more defects, black dots, and darker areas due to the bigger size of the nanoparticles and bigger agglomerates formed on the modified surfaces, a well-defined layered structure up to the seventh layer and a slight coalescence of the structural elements after the eighth layer adsorbed on the surface (result not shown). This is in good agreement with the literature, and as an example to be mentioned, Rubinstein et al. have also observed a regular growth and a compact structure after nine layers of Au NPs have been constructed on gold substrates using coordination chemistry.^{8,9}

3.3. Electrochemical Characterization of Poly(L-arginine)/Au–MUA NP Multilayers Using [Fe(CN)₆]^{3-/4-} as the Electroactive Species. The electrical features of the multilayered poly(L-arginine)/Au–MUA NP assemblies were elucidated by cyclic voltammetry, square wave voltammetry, and electrochemical impedance spectroscopy. Figure 5 shows the CVs measured on the multilayer modified gold electrode for the redox couple [Fe(CN)₆]^{3-/4-}. Compared with the previous type of multilayer composed of poly(L-lysine) and gold nanoparticles stabilized with mercaptosuccinic acid and studied in the same conditions,³⁴ it is interesting to remark the different response of the poly(L-arginine)/mercaptoundecanoic acid derivatized gold nanoparticle multilayer modified electrode toward negatively charged species in solution. In this case, the only layer with increased peak-to-peak separation and diminished peak currents is the MSA layer (*n* = 1) as seen previously. The multilayers with odd values of *n* (Au–MUA NPs layers, Figure 5a) exhibit a different behavior then expected: increased peak currents and decreased peak separation. The corresponding peak-to-peak separations are 0.092 V for *n* = 0 (bare gold), 0.191 V for *n* = 1 (MSA on gold), 0.085 V for *n* = 3 (first Au NPs layer), 0.082 V for *n* = 5 (the second Au NPs layer), 0.084 V for *n* = 7 (the third Au NPs layer), and 0.083 V for *n* = 9 (the fourth Au NPs layer). Previous studies indicated that the electron transfer at charged interfaces is controlled by electrostatic

attraction or repulsion of the solubilized charged redox probes.^{34,38–41} That is, attraction of a positively charged species to a negatively charged interface enhances the interfacial electron transfer, whereas the repulsion of a negatively charged redox label leads to a barrier for the redox process that is reflected by an increased charge-transfer resistance at the modified electrode (Frumkin effect).⁴² In this work, although the redox probes are negatively charged, for Au NP terminated multilayers (negatively charged surfaces) the peak current in the cyclic voltammograms increases and semi-infinite planar diffusion begins to take place. A slight blocking of the electrode surface is observed only after the deposition of seven and nine layers (Figure 5a, *n* = 7, 9, Au NP terminated multilayers) depicted through a slight decrease of the peak currents, but the electrochemical process is still highly favored by the Au NP terminated multilayer. This indicates that the charge transfer seems to be at least as fast in the outer layers as in the inner layers. Otherwise, if a significant resistance would be added by each layer, the peak separation should increase. This effect could be due to the bigger size of the Au NPs (3.0 nm average diameters) within this new multilayer which determines a faster electron transfer, so implying a catalytic behavior of the clusters. Also the long chain of the MUA on the nanoparticles surface implies that the negative charge (COO[−] groups) is far from the clusters surface; in consequence, the repelling effect between the negatively charged surface and the redox probes is drastically decreased. On the Au–MUA NPs surface, the carboxylate groups are at least 15.4 Å away from the surface when compared with the MSA on gold clusters for which the farthest COO[−] group is at approximately 3.08 Å (taking into account only the C–C length⁴³ which is 1.54 Å). This may explain the different electrical properties of Au–MUA NP terminated multilayers compared to Au–MSA NP terminated multilayers self-assembled on gold electrodes, when [Fe(CN)₆]^{3-/4-} species are used as the redox probes. A similar behavior is observed for even values of *n* (Figure 5b). The outer pArg layer (positively charged surfaces) enhances the concentration of electroactive species within the film by means of the Donnan inclusion which leads to quasireversible cyclic voltammograms with high peak currents and decreased peak separation. In this situation the peak-to-peak separations in the CVs recorded for each outermost layer of pArg are also slightly improved compared with the bare gold, being 0.079 V for *n* = 2 (the first pArg layer), 0.077 V for *n* = 4 (the second pArg layer), 0.076 V for *n* = 6 (the third pArg layer), 0.074 V for *n* = 8 (the fourth pArg layer), and 0.082 V for *n* = 10 (the fifth pArg layer).

Further characterization of the multilayers was performed by using square wave voltammetry which represents a voltammetric technique with high sensitivity to surface-confined electrode reaction. Figure 6 shows the square wave voltammograms (net currents) recorded at the pArg/Au–MUA NP modified electrode in an aqueous solution of [Fe(CN)₆]^{3-/4-} and NaClO₄ used as supporting electrolyte.

As seen previously, the presence of the MSA layer (Figure 6a, *n* = 1) is portrayed by diminished peak currents of the square wave voltammogram and by shifting of the square wave peak potential in the positive direction (i.e., the oxidation process is hindered and higher positive overpotential is required for its occurrence). This behavior implies a slow electron transfer at the MSA modified electrode.⁴⁴ The first pArg layer (Figure 6b, *n* = 2) regains the quasireversible response in the square wave voltammograms due to the electrostatic attractive interaction toward the negatively charged [Fe(CN)₆]^{3-/4-} probes. The next deposited layer (Au NP layer, Figure 6a, *n* = 3) determines a

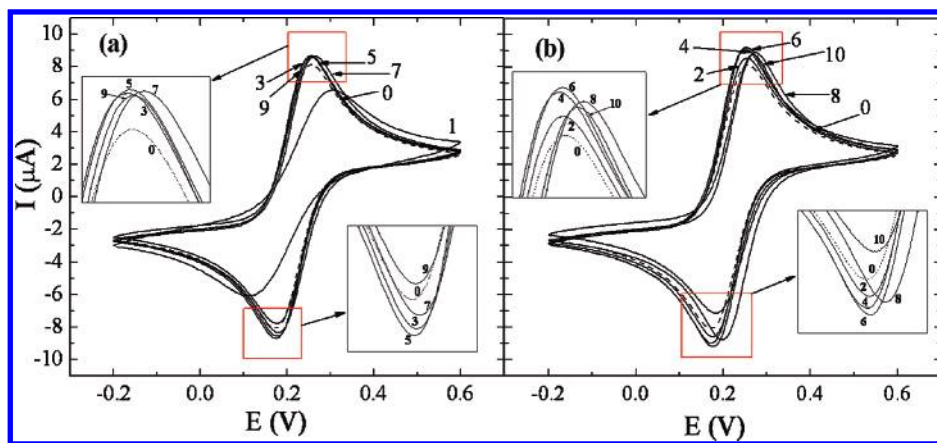


Figure 5. Cyclic voltammograms of the pArg/Au-MUA NP multilayer modified electrode in a 0.1 M NaClO₄ aqueous solution containing 1 mM [Fe(CN)₆]^{3−} and 1 mM [Fe(CN)₆]^{4−}: (a) first MSA layer ($n = 1$) and Au-MUA NPs terminated multilayers with $n = 3, 5, 7$, and 9 layers; (b) poly(L-arginine) terminated multilayers with $n = 2, 4, 6, 8$, and 10 layers. The bare electrode curve (dashed line, $n = 0$) is shown for comparison. The scan rate is 50 mV/s.

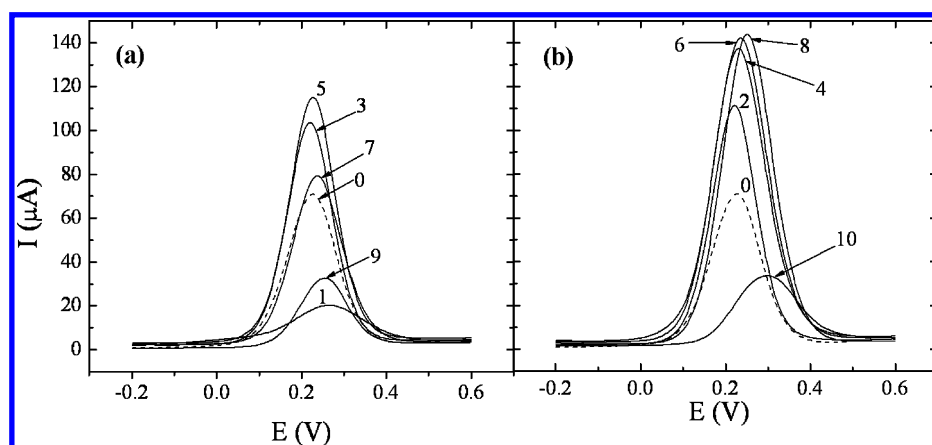


Figure 6. Square wave voltammograms (net currents) of the multilayer modified electrode in a 0.1 M NaClO₄ aqueous solution containing 1 mM [Fe(CN)₆]^{3−} and 1 mM [Fe(CN)₆]^{4−}. The starting potential was -0.2 V. The number of layers deposited is indicated in the figures.

slight decrease of the peak current compared to the previous pArg layer, but the modified electrode shows better electrical properties than the bare electrode. Further buildup of the poly(L-arginine) and Au-MUA NP layers results in continuation of this behavior. A more compact structure of the film is attained after the deposition of the last two layers (Figure 6, $n = 9, 10$) on the electrode surface which determines a decrease of the square wave peak current compared to the bare electrode and a shift of the square wave peak potential toward more positive values. At this stage of the multilayer buildup, the electrode surface starts to be blocked and the electrochemical process to be hindered although the last layer deposited is a polymer layer which could still enhance the concentration of the electroactive species into the film. Compared to the bare electrode, the peak currents obtained for the Au-MUA NP terminated multilayers increase by 45% (Figure 6a, $n = 5$) while the peak currents obtained for the pArg terminated multilayers increase by 73% (Figure 6b, $n = 8$). This new multilayer shows reversible cyclic and square wave voltammograms for all the layers which is a very promising feature for the electrochemical sensing of different compounds in solution. The presence of gold nanoparticles improves the conductivity and the electron-transfer ability of the film.

The Nyquist plots at different stages of the multilayer growth are displayed in Figure 7. The fitting of the data was performed using nonlinear least-square fit, and the parameter values, given in Table 4, agree very well with the experimental EIS spectra. The equivalent electrical circuit used previously for the fitting

of the impedance spectra^{34,38} was reduced either to the Randles circuit for $n = 0, 3, 5$ (bare electrode and the Au NP terminated multilayer) or to a simpler equivalent circuit, represented in Figure 8, for $n = 2, 4, 6$, and 8 (pArg terminated multilayer). The equivalent electrical circuit used in the capillary membrane model³⁸ (CMM) was applied for the fitting of the impedance spectra of the first layer ($n = 1$, MSA layer), the 7th, 9th, and 10th layers self-assembled on the gold electrode ($n = 7, 9$, Au NP terminated multilayer and $n = 10$, pArg terminated multilayer). As it can be observed from the Nyquist diagrams (Figure 7a, right inset), an Au electrode modified with a mercaptosuccinic acid monolayer ($n = 1$) shows high semicircle at high frequencies which is consistent with an increased charge-transfer resistance compared to the bare electrode, due to electrostatic repulsion of the redox label, [Fe(CN)₆]^{3−/4−}. The subsequent assembly of the first layer of poly(L-arginine) (Figure 7b, $n = 2$) cancels the interfacial charge-transfer resistance of the previous layer, due to the electrostatic attractive interaction toward the redox probe. Addition of a third layer consisting of negatively charged Au-MUA NPs (Figure 7a, $n = 3$) involves a very small charge-transfer resistance (see Table 4), and the binding of the fourth layer of positively charged pArg (Figure 7b, $n = 4$) again nullifies the interfacial electron-transfer resistance. Further buildup of the assembly shows similar behavior until the deposition of 9 layers (Figure 7a, $n = 9$, Au-MUA NP terminated multilayer) and 10 layers (Figure 7b, inset, $n = 10$, pArg terminated multilayer) for which the charge-transfer resistance is higher than for the bare electrode (high

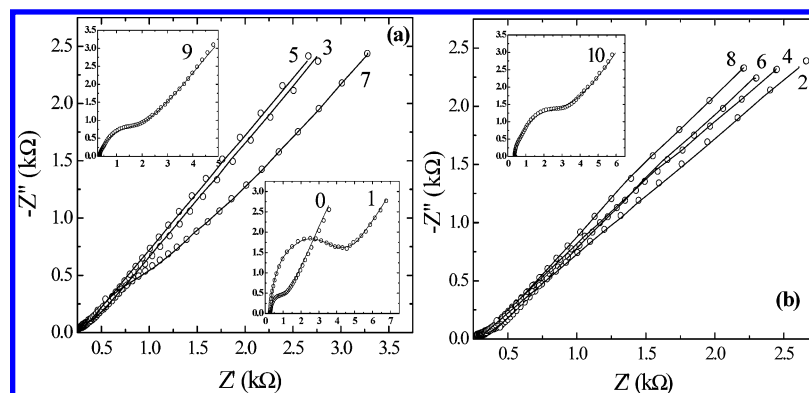


Figure 7. Nyquist diagrams of poly(L-arginine)/Au-MUA NP multilayer modified electrode in a 0.1 M NaClO₄ aqueous solution containing 1 mM [Fe(CN)₆]³⁻ and 1 mM [Fe(CN)₆]⁴⁻. The number of layers n is indicated close to the curves. The experimental data are represented by circles and the fitted data by solid lines.

TABLE 4: Parameter Values Obtained from the Fittings of the Impedance Spectra in Figure 7 Using Nonlinear Least-Square Fit^a

n	R_s (kΩ)	C_f (μF)	R_f (kΩ)	C_{dl} (μF)	R_{CT} (kΩ)
0	0.30 (0.82)			1.20 (0.63)	0.70 (1.30)
1	0.29 (0.84)	1.03 (1.05)	1.6 (1.21)	1.09 (0.56)	3.15 (1.53)
pArg Terminated Multilayer					
2	0.29 (1.29)	1.35 (1.2)	0.09 (3.2)	2.65 (2.50)	
4	0.27 (0.98)	1.62 (3.1)	0.12 (2.0)	6.42 (4.12)	
6	0.28 (1.63)	1.28 (0.54)	0.15 (3.08)	8.53 (3.58)	
8	0.30 (1.68)	3.82 (1.29)	0.14 (1.76)	12.73 (3.72)	
10	0.35 (1.98)	4.12 (0.86)	0.16 (1.79)	8.25 (1.98)	1.52 (2.35)
Au-MUA NP Terminated Multilayer					
3	0.26 (0.86)			0.67 (2.60)	0.06 (0.95)
5	0.27 (0.49)			1.12 (1.32)	0.11 (0.70)
7	0.31 (0.88)	1.55 (1.35)	0.22 (1.63)	3.75 (2.62)	0.40 (0.85)
9	0.33 (1.35)	0.73 (1.45)	0.48 (3.16)	1.33 (4.52)	0.90 (3.21)

^a The percent errors from the fit for each element are given in parentheses.

semicircles at high frequencies) and the peak currents of the cyclic and square wave voltammograms are lower (Figures 5 and 6). At this stage of the multilayer buildup, the elevated thickness of the film starts to block the surface and to hinder the electrochemical process. At low frequency, the slope of the impedance plots is close to unity, thus indicating semi-infinite planar diffusion to the film. The charge-transfer resistance can be translated into the exchange current under equilibrium I_0 using

$$R_{CT} = \frac{RT}{nFI_0} \quad (1)$$

And further, the experimental heterogeneous electron-transfer rate constant, k_{exp} , can be evaluated using

$$I_0 = nFAk_{exp}[c] \quad (2)$$

where R is the gas constant, T is the temperature (K), A is the electrode area (cm²), $[c]$ corresponds to the bulk concentration

of the redox probe (mol·cm⁻³), and n is the number of transferred electrons per molecule of the redox probe ($n = 1$ for the [Fe(CN)₆]^{3-/4-} probes).

For example, the observed charge-transfer resistances for the bare electrode and the third, fifth, and seventh layers of Au-MUA NPs are 0.70, 0.06, 0.11, and 0.4 kΩ, respectively, and give heterogeneous electron-transfer rate constants of 0.126×10^{-3} , 14.7×10^{-3} , 8×10^{-3} , and 2.2×10^{-3} cm·s⁻¹, respectively, which confirm the catalytic effect of the gold clusters within the multilayered film.

The double layer capacitance, C_{dl} , depends also on the dielectric and insulating features at the electrode/electrolyte interface and is controlled by the electrode surface modification. For both types of layers, C_{dl} shows increasing values. For the pArg terminated multilayer, both the film resistance R_f and the film capacitance C_f increase with the number of layers n , indicating that the film area is increasing as well as the compactness of the multilayer. The estimated electrode coverage θ for the first layer ($n=1$, MSA layer) calculated using the eq 3 is 78% of the electrode area.³⁸ As seen in the AFM images

$$(1 - \theta) = \frac{R_{CT, bare}}{R_{CT, layer}} \quad (3)$$

(Figure 4), both the Au-MUA NPs layers and the poly(L-arginine) layers cover quite uniformly the surface of the gold slides which can be an indication that the coverage of the electrode is progressively increased as more layers are added, and this is well sustained by the increasing film capacitance, C_f , with increasing n . For the Au-MUA NP terminated multilayer, there is no variation of the capacitance of the film, C_f , or resistance of the film, R_f , until the seventh layer of the multilayer composite. This is due to the large electronic overlap between the layers of the nanoparticles which are interconnected both laterally and perpendicularly favoring the electron transfer.

As mentioned previously, the increased size of the nanoparticles improves the electrical properties of the film, and possibly, the longer chain of the ligand on the clusters reduces drastically the repelling effect between the negatively charged Au-MUA NPs as outermost layers and the [Fe(CN)₆]^{3-/4-} as the redox probes in solution. The fact that the guanidino group of pArg has a planar geometry with delocalized charge should also favor better interaction between these groups and the COOH groups of the Au-MUA NPs thus leading to an increased amount of pArg deposited when compared to pLys. As seen previously, when the electroactive species are negatively charged, it is plausible to observe a higher current for even values of n than for odd values of n ,³⁵ but the current increases with the number

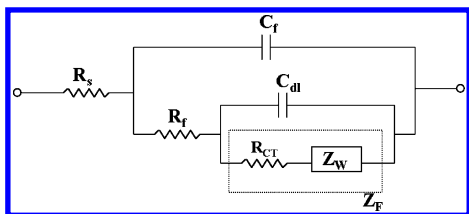


Figure 8. Equivalent electrical circuit used for the fitting of the impedance spectra represented in Figure 7.

of layers (for NPs terminated films, $n = 3, 5, 7$) which suggests that the sensitivity of the electrode is improved by the Au–MUA NP layers. In this case, the hydrophobic nature of the ligand on the nanoparticle surface could determine a decrease of the concentration of the electroactive species in the film which could explain the smaller peak currents in the square wave voltammograms for the Au–MUA NP terminated multilayers than for the pArg terminated multilayers. Reversely, higher peak currents in the cyclic and square wave voltammograms for pArg terminated multilayers are due to the Donnan inclusion of the redox probes but also due to the cumulative contribution of the electron transfer mediated by the Au NPs from the inner layers.

This is consistent with previous works which report electrochemical sensing of hydroquinone at a citrate Au nanoparticles multilayered modified ITO electrode⁴⁵ or a similar electrochemical response toward $[\text{Fe}(\text{CN})_6]^{3-/4-}$ probes in solution at a glassy carbon electrode modified with multiwall carbon nanotubes.⁴⁶ Overall, the film properties are improved compared to our previous study on films composed of a pLys/Au–MSA NP multilayer which represents great possibilities for electronic applications and sensing.

Conclusions

Carboxylic-capped gold nanoparticles with sizes from 1.0 to 4.0 nm were synthesized based on the reduction of hydrogen tetrachloroaurate(III) by sodium borohydride in methanol using mercaptoundecanoic acid as the stabilizing thiol ligand. The clusters were characterized by UV–vis spectroscopy, transmission electron microscopy, ζ -potential measurement, and Fourier transform-infrared spectroscopy. The results show that the particles have quasispherical shapes and monodisperse sizes, and the ligands on their surface exist as carboxylic acids. As proven by ζ -potential measurements, the Au–MUA NPs powders dissolved in aqueous TEAOH were negatively charged. Au–MUA NPs of 3.0 nm average diameters were used for the construction of layer-by-layer self-assembled multilayers using poly(L-arginine) as a polycation. The polymer/gold cluster composite was characterized by using UV–vis spectroscopy, atomic force microscopy, cyclic voltammetry, square wave voltammetry, and electrochemical impedance spectroscopy. The charge transport mechanism was studied experimentally by using $[\text{Fe}(\text{CN})_6]^{3-/4-}$ as a redox probe. On the basis of the EIS and voltammetry studies, we conclude that the main charge transport mechanism for Au–MUA NPs terminated multilayers in the presence of the redox probe $[\text{Fe}(\text{CN})_6]^{3-/4-}$ is electron transport mediated by the Au NPs. In the case of pArg terminated multilayers, the main charge transport mechanism is ionic diffusion due to the electrostatic attractive interaction with the redox probe which diffuses freely into the polymer matrix and further into the film structure. Overall, this multilayer composite showed a high permeability to the probe ions depicted through reversible cyclic voltammograms with high peak currents and decreased peak separation, reversible square wave voltammograms with high peak currents, and EIS spectra with very low

charge-transfer resistance controlled mainly by the increasing film thickness. Interestingly, the permeability of the film increased with an increasing number of layers. The results proved also a high catalytic effect of the gold nanoparticles used for the multilayer construction depicted by a faster electron transfer on the multilayered modified electrode than on the bare electrode. Broad applications are envisaged for this type of film: the construction of highly conductive electronic nanodevices or the development of sensors for the electrochemical detection of different compounds in solution. We are currently exploring further the electrochemical properties of these new films.

Acknowledgment. M.C. thanks Timo Laaksonen from Helsinki University of Technology, Finland, for the measurements with transmission electron microscopy. Financial support from the European Union under the network SUSANA (“Supramolecular Self-Assembly of Interfacial Nanostructures”, Contract No. HPRN-CT-2002-00185) is gratefully acknowledged.

Supporting Information Available: FT-IR spectra of the mercaptoundecanoic acid and gold nanoparticles stabilized with mercaptoundecanoic acid, tapping mode AFM images of the MSA layer and the first poly(L-arginine) layer, tapping mode AFM images of pArg as the fourth layer and Au–MUA NPs as the fifth layer within the multilayers with colloids of 1.0, 3.0, and 4.0 nm average diameters. This material is available free of charge via the Internet at <http://pubs.acs.org>.

References and Notes

- (1) Joseph, Y.; Krasteva, N.; Besnard, I.; Guse, B.; Rosenberger, M.; Wild, U.; Knop-Gericke, A.; Schlögl, R.; Krustev, R.; Yasuda, A.; Vossmeier, T. *Faraday Discuss.* **2004**, *125*, 77.
- (2) Yang, W.; Wang, J.; Zhao, S.; Sun, Y.; Sun, C. *Electrochem. Commun.* **2006**, *8*, 665.
- (3) Stanca, S.-E.; Eritja, R.; Fitzmaurice, D. *Faraday Discuss.* **2006**, *131*, 155.
- (4) Abdelrahman, A. I.; Mohammad, A. M.; Okajima, T.; Ohsaka, T. *J. Phys. Chem. B* **2006**, *110*, 2798.
- (5) Yang, W.; Li, Y.; Bai, Y.; Sun, C. *Sens. Actuators, B* **2006**, *115*, 42.
- (6) Liu, Y.; Yuan, R.; Chai, Y.; Tang, D.; Dai, J.; Zhong, X. *Sens. Actuators, B* **2006**, *115*, 109.
- (7) Song, Y.; Wang, L.; Ren, C.; Zhu, G.; Li, Z. *Sens. Actuators, B* **2006**, *114*, 1001.
- (8) Wanunu, M.; Vaskevich, A.; Cohen, S. R.; Cohen, H.; Arad-Yellin, R.; Shanzer, A.; Rubinstein, I. *J. Am. Chem. Soc.* **2005**, *127*, 17877.
- (9) Wanunu, M.; Popovitz-Biro, R.; Cohen, H.; Vaskevich, A.; Rubinstein, I. *J. Am. Chem. Soc.* **2005**, *127*, 9207.
- (10) Ung, T.; Liz-Marzán, L. M.; Mulvaney, P. *J. Phys. Chem. B* **2001**, *105*, 3441.
- (11) Yu, A. M.; Liang, Z. J.; Cho, J. H.; Caruso, F. *Nano Lett.* **2003**, *3*, 1203.
- (12) Shipway, A. N.; Katz, E.; Willner, I. *Chem. Phys. Chem.* **2000**, *1*, 18 and references therein.
- (13) Daniel, M.-C.; Astruc, D. *Chem. Rev.* **2004**, *104*, 293.
- (14) Maye, M.; Lou, Y.; Zhong, C.-J. *Langmuir* **2000**, *16*, 7520–7523.
- (15) Biswas, P. C.; Nodasaka, Y.; Enyo, M.; Haruta, M. *J. Electroanal. Chem.* **1995**, *381*, 167.
- (16) Yu, A. M.; Liang, Z. J.; Cho, J. H.; Caruso, F. *Nano Lett.* **2003**, *3*, 1203.
- (17) Valden, M.; Lai, X.; Goodman, D. W. *Science* **1998**, *281*, 1647.
- (18) Fan, H. Y.; Yang, K.; Boye, D. M.; Sigmon, T.; Malloy, K. J.; Xu, H. F.; Lopez, G. P.; Brinker, C. J. *Science* **2004**, *304*, 567–571.
- (19) Rowe, M. P.; Plass, K. E.; Kim, K.; Kurdak, C.; Zellers, E. T.; Matzger, A. J. *Chem. Mater.* **2004**, *16*, 3513–3517.
- (20) Sagara, T.; Kato, N.; Nakashima, N. *J. Phys. Chem. B* **2002**, *106*, 1205–1212.
- (21) Freeman, R. G.; Grabar, K. C.; Allison, K. J.; Bright, R. M.; Davis, A. J.; Guthrie, A. P.; Hommer, M. B.; Jackson, M. A.; Smith, P. C.; Walter, D. G.; Natan, M. J. *Science* **1995**, *267*, 1629–1635.
- (22) Chan, E. W. L.; Yu, L. *Langmuir* **2002**, *18*, 311–313.

- (23) Patton, D.; Locklin, J.; Meredith, M.; Xin, Y.; Advincula, R. *Chem. Mater.* **2004**, *16*, 5063.
- (24) Santos, H. A.; Chirea, M.; Morales, V. G.; Silva, F.; Manzanares, J. A.; Kontturi, K. *J. Phys. Chem. B* **2005**, *109*, 20105.
- (25) Hu, X.; Cheng, W.; Wang, T.; Wang, Y.; Wang, E.; Dong, S. *J. Phys. Chem. B* **2005**, *109*, 19385.
- (26) Jiang, H.; Su, W.; Hazel, J.; Grant, J. T.; Tsukruk, V. V.; Cooper, T. M.; Bunning, T. J. *Thin Solid Films* **2000**, *372*, 85.
- (27) Kurth, D. G.; Volkmer, D.; Ruttorf, M.; Richter, B.; Muller, A. *Chem. Mater.* **2000**, *12*, 2829.
- (28) Caruso, F.; Niikura, K.; Furlong, D. N.; Okahata, Y. *Langmuir* **1997**, *13*, 3427.
- (29) Hicks, J. F.; Young, S.-S.; Murray, R. W. *Langmuir* **2002**, *18*, 2288.
- (30) Feldheim, D. L.; Grabar, K. C.; Natan, M. J.; Mallouk, T. E. *J. Am. Chem. Soc.* **1996**, *118*, 7640.
- (31) Song, W.; Okamura, M.; Kondo, T.; Uosaki, K. *Phys. Chem. Chem. Phys.* **2003**, *5*, 5279.
- (32) Xiao, Y.; Patolsky, F.; Katz, E.; Hainfeld, J. F.; Willner, I. *Science* **2003**, *299*, 1877.
- (33) Zhang, Y. R.; Asahina, S.; Yoshihara, S.; Shirakashi, T. *Electrochim. Acta* **2003**, *48*, 741.
- (34) Chirea, M.; Morales, V. G.; Manzanares, A. J.; Pereira, C.; Gulaboski, R.; Silva, F. *J. Phys. Chem. B* **2005**, *109*, 21808.
- (35) Chen, S.; Kimura, K. *Langmuir* **1999**, *15*, 1075.
- (36) Kim, K.-H.; Yamada, M.; Park, D.-W.; Miyake, M. *Chem. Lett.* **2004**, *33*, 344.
- (37) Shia, W.; Sahoob, Y.; Swiharta, M. T.; *Colloids Surf., A*: **2004**, *246*, 109.
- (38) Barreira, S. V. P.; García-Morales, V.; Pereira, C. M.; Manzanares, J. A.; Silva, F. *J. Phys. Chem. B* **2004**, *108*, 17973.
- (39) Pardo-Yissar, V.; Katz, E.; Lioubashevski, O.; Willner, I. *Langmuir* **2001**, *17*, 1110.
- (40) Katz, E.; Willner, I. *Electroanalysis* **1995**, *7*, 417.
- (41) Katz, E.; Lion-Dagan, M.; Willner, I. *J. Electroanal. Chem.* **1996**, *408*, 107.
- (42) Delahay, P. *Double Layer and Electrode Kinetics*; Interscience: New York, 1965.
- (43) Morrison, R. T.; Boyd, R. N.; Boyd, R. K. *Organic Chemistry*, 6th ed.; Prentice Hall, Inc.: Englewood Cliffs, NJ, 1992.
- (44) Osteryoung, J.; O'Dea, J. J. *Square-Wave Voltammetry*. In *Electroanalytical Chemistry*; Bard, A. J., Ed.; Marcel Dekker: New York, 1986; Vol. 14, p 209.
- (45) Shipway, A. N.; Lahav, M.; Blonder, R.; Wilner, I. *Chem. Mater.* **1999**, *11*, 13.
- (46) Acevedo, D. F.; Balach, J.; Rivarola, C. R.; Miras, M. C.; Barbero, C. A. *Faraday Discuss.* **2006**, *131*, 235.